



Contents lists available at ScienceDirect

## Journal of Volcanology and Geothermal Research

journal homepage: [www.elsevier.com/locate/jvolgeores](http://www.elsevier.com/locate/jvolgeores)

## Staged storage and magma convection at Ambrym volcano, Vanuatu

Fionnuala Sheehan\*, Jenni Barclay

University of East Anglia, Norwich NR4 7TJ, UK

## ARTICLE INFO

## Article history:

Received 1 July 2015

Received in revised form 22 February 2016

Accepted 23 February 2016

Available online xxx

## Keywords:

Ambrym

Thermobarometry

Petrology

Recharge

Convection

Mafic

## ABSTRACT

New mineral-melt thermobarometry and mineral chemistry data are presented for basaltic scoriae erupted from the Mbwelesu crater of Ambrym volcano, Vanuatu, during persistent lava lake activity in 2005 and 2007. These data reveal crystallisation conditions and enable the first detailed attempt at reconstruction of the central magma plumbing system of Ambrym volcano. Pressures and temperatures of magma crystallisation at Ambrym are poorly constrained. This study focuses on characterising the magma conditions underlying the quasi-permanent lava lakes at the basaltic central vents, and examines petrological evidence for magma circulation. Mineral-melt equilibria for clinopyroxene, olivine and plagioclase allow estimation of pressures and temperatures of crystallisation, and reveal two major regions of crystallisation, at 24–29 km and 11–18 km depth, in agreement with indications from earthquake data of crustal storage levels at c. 25–29 km and 12–21 km depth. Temperature estimates are ~1150–1170 °C for the deeper region, and ~1110–1140 °C in the mid-crustal region, with lower temperatures of ~1090–1100 °C for late-stage crystallisation. More primitive plagioclase antecrysts are thought to sample a slightly more mafic melt at sub-Moho depths.

Resorption textures combined with effectively constant mafic mineral compositions suggest phenocryst convection in a storage region of consistent magma composition. In addition, basalt erupted at Ambrym has predominantly maintained a constant composition throughout the volcanic succession. This, coupled with recurrent periods of elevated central vent activity on the scale of months, suggest frequent magmatic recharge via steady-state melt generation at Ambrym.

© 2016 The Authors. Published by Elsevier B.V. This is an open access article under the CC BY license (<http://creativecommons.org/licenses/by/4.0/>).

## 1. Introduction

Ambrym is one of the most active volcanoes in the Vanuatu island arc, SW Pacific. It has been continuously active since first described in 1774, displaying persistent lava lake activity, gas bursting (cf. Harris and Ripepe, 2007), and prodigious outgassing (Bani et al., 2009, 2012), with intermittent explosive or lava flow events.

Ambrym features long-lived lava lakes in two adjacent near-summit intracaldera cones. The volume of historically erupted magma at Ambrym volcano is low, but the presence of quasi-permanent lava lakes and long-lived high gas output require sustained heat and gas fluxes (Harris et al., 1999), and imply magma recycling (Harris et al., 1999), endogenous growth (Francis et al., 1993; Oppenheimer and Francis, 1998), or cryptic intrusion (Harris and Stevenson, 1997). Periodic decrease of lava-lake levels at Ambrym, without any significant extrusion of lava, may indicate that magma drains back into the crustal storage system from high levels, or may also reflect decrease in conduit magma volume due to loss of gas bubbles. Following descent, degassed magma is presumed to mix with reservoir magma, or to crystallise cumulates (cf. Harris et al., 1999). Elevated lava lake activity, such as

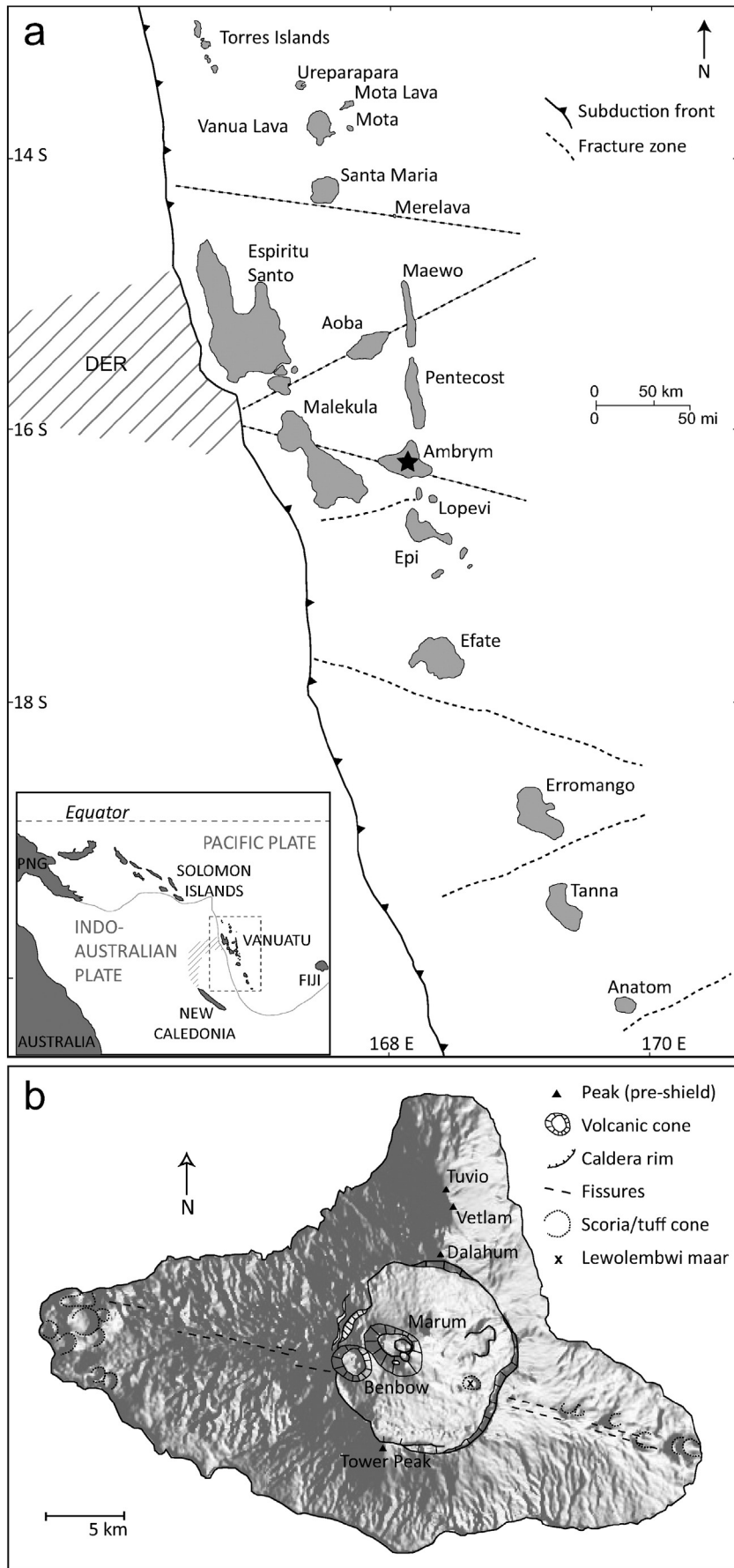
in the current phase, features vigorous convection and gas bursting at the lake surface, indicating that ascent of gas-rich magma drives elevations in lava lake levels.

Persistent lava lakes, on the scale of years to decades, have been recorded in only a handful of other locations: Kilauea (Hawai'i), Erebus (Antarctica), Erta' Ale (Ethiopia), Masaya (Nicaragua), Nyiragongo (Democratic Republic of the Congo), and Villarica (Chile), and are a relatively lesser-studied phenomenon given their rarity and low hazard potential. Satellite-based mass flux estimates (Wright and Pilger, 2008) indicate that magma flux at Ambrym (~5–65 kg s<sup>-1</sup> or 20–360 kg s<sup>-1</sup>, depending on the model used) is comparable to that for active lava lakes at Erta' Ale (Ethiopia) and Erebus (Antarctica) volcanoes. Using the petrological method, Allard et al. (2015) calculated a 'spectacularly high' magma supply rate of 25 m<sup>3</sup> s<sup>-1</sup>, four times greater than that estimated at Kilauea and six times higher than that estimated for Etna. These findings indicate that Ambrym is a striking and possibly even extreme example of a basaltic system with a very high magma supply rate.

In addition to degassing and lava lake activity, Ambrym features recurrent paroxysms on a timescale of years. Paroxysms at basaltic volcanoes cause intermittent elevation of volcanic hazard associated with systems which are otherwise typically considered to be relatively safe to approach. Prominent examples of this type of volcano include

\* Corresponding author.

E-mail address: [fionnuala.sheehan@gmail.com](mailto:fionnuala.sheehan@gmail.com) (F. Sheehan).



Stromboli (Italy) and Yasur (Vanuatu): both popular tourist destinations, with concomitant implications for hazard. Ambrym is another such system. Ambrym is becoming increasingly popular as an adventure destination, with an attendant increase in hazard, both for tourists and for the island inhabitants who guide them to the active intracaldera vents. Significant increases in activity can impact the wider island community, who live in villages concentrated along the coast. Episodes of heavy degassing create acid rain, which damages crops, and human and livestock health (Cronin and Sharp, 2002). Hazards associated with these fluctuating modes of magmatism can be mitigated given improved understanding of the driving mechanisms of variations in activity.

The relationship of magma recharge to the timing of eruptions, and the cause of transition to paroxysmal activity at basaltic volcanoes, e.g. at Stromboli (e.g. Bertagnini et al., 2011) and Etna (e.g. Allard et al., 2006), is not fully resolved. This study represents a first step towards petrologically characterising magma conditions related to variations in modes of activity at Ambrym. Inferences relating to lava lake activity can be compared and contrasted to products of paroxysmal events to evaluate controls on changes in eruptive regime.

## 2. Geology and eruptive history

Ambrym is a large pyroclastic shield volcano located in the central chain of the Vanuatu arc, adjacent to the D'Entrecasteaux Zone, where an aseismic ridge (the D'Entrecasteaux Ridge) collides with the arc (Fig. 1a). The ESE-elongated morphology of the island (Fig. 1b) is believed to reflect the influence of a regional compressive stress cause by the D'Entrecasteaux Zone collision (Greene et al., 1988).

The earliest stage of volcanism is represented by a handful of peaks (Tuvio, Vetlam, and Dalahum) on a north–south lineation, overlain by a basaltic shield, itself topped by a voluminous basaltic-to-dacitic pyroclastic sequence with a 12 km diameter summit caldera which formed c. 2 Ka (Robin et al., 1993). Two long-lived basaltic cones, Marum and Benbow, have developed inside the caldera; these are the primary locus of current activity (Fig. 1b). The predominant mode of volcanism comprises strong degassing and quasi-permanent lava-lake activity of variable intensity from Marum and Benbow, with heavy degassing—“great columns of smook”—noted by Captain Cook in the earliest recorded description of Ambrym, in 1774. This is punctuated by occasional (seven reported since 2004) low-altitude (<3 km) ash plumes and minor paroxysms, sometimes accompanied by overflow of lava from the intracaldera cones and lava emission via flank fissures. There have been 54 of these minor paroxysms in the 240 years since records began; an average of one every ~4 years (Global Volcanism Program, 2013). These events are usually VEI 2 (69% of events); occasionally VEI 3 (13% of events); and on only one occasion as high as VEI 4. These eruptions can cause disruption to sectors of the island population (7275 people; Vanuatu National Statistics Office, 2009) through explosive hydrovolcanism, lava flows, ash fall, and acid rain, which causes crop damage, contamination of water supplies, skin burns and fluorosis (Cronin and Sharp, 2002). Over the last 60 years, these episodes of heightened activity have been generally non-destructive, in that they are confined to the summit caldera, and affect the primarily coastal population only via ash fallout and acid rainfall. Far more destructive events have occurred on occasion, however: in 1913 a coastal mission hospital, and the land on which it stood, were completely destroyed (Gregory, 1917), killing 21 people and injuring c. 121 (Witham, 2005), when a flank eruption became phreatomagmatic on approaching the coast

(Németh and Cronin, 2011). Eleven events affecting the extracaldera area have occurred since 1820, and partial evacuations occurred in 1913–15, 1929, and 1951 (Eissen et al., 1991). Activity has been confined to the caldera since 1942.

The geological development of Ambrym has occurred in four geochemically distinct volcanic phases (Fig. 2a): the earliest (Pleistocene) edifices, Tuvio, Vetlam and Dalahum, in which the most primitive products are found, with 12.8 wt.% MgO and 49.1 wt.% SiO<sub>2</sub>; the significantly less primitive basaltic shield with ≤5.2 wt.% MgO; the basaltic-to-rhyodacitic Ambrym Pyroclastic Series (APS) associated with caldera formation ~2 Ka; and post-caldera, primarily basaltic activity, from 2 Ka to present (Picard et al., 1995).

The erupted products are compositionally bimodal (Fig. 2b), but are primarily basalt to basaltic andesite (Fig. 2c), with the majority of compositions falling between 49 and 54 wt.% SiO<sub>2</sub> and a much smaller cluster around 66 wt.% SiO<sub>2</sub> (Picard et al., 1995). A trachyandesite lava (~60 wt.% SiO<sub>2</sub>) erupted in the eastern part of the caldera in 1986 is the only ‘evolved’ post-caldera product, and one of only a handful of non-basaltic products throughout the entire history of the volcano. Andesitic to rhyodacitic pyroclastics are found in the mainly basaltic pyroclastic series, and a glassy andesitic lava flow believed to relate to caldera formation occurs at the northern rim of the caldera (Picard et al., 1995). The 1986 trachyandesite is the only recorded relatively-evolved product not related to pyroclastic series or caldera formation.

It can be seen from Fig. 2a that the earliest, most primitive lavas gave way to a predominant basaltic composition by the shield stage, and that the system has subsequently maintained this predominant composition throughout the volcanic succession, with only minor incidences of more primitive (post-caldera olivine basalts) or more silicic (pyroclastic series andesite to rhyodacite, and post-caldera trachyandesite) compositions. The phenocryst assemblage, as reported by Picard et al. (1995), has remained remarkably similar from earliest to recent times: in the most primitive lavas (TVD), phenocryst compositions are normally-zoned plagioclase of An<sub>82–55</sub>, augite, olivine (Fo<sub>83–79</sub>) and Fe–Ti oxides; the basal shield is composed of basalt with normally-zoned plagioclase of An<sub>91–67</sub>, augite, normally-zoned olivine of Fo<sub>84(cores)–51(rims)</sub> and Fe–Ti oxides; and post-caldera basalts contain normally-zoned plagioclase (An<sub>92–65</sub>), augite, normally-zoned olivine (Fo<sub>78–55</sub>), and Fe–Ti oxides, in a plagioclase-rich (An<sub>70–60</sub>) groundmass. All are also characterised by a glomeroporphyritic texture.

### 2.1.1. Existing constraints on magma storage conditions

Existing constraints on magma storage conditions at Ambrym derive primarily from geophysical investigations and seismic studies.

Several studies have indicated that Ambrym and Benbow share the same magma body at depth, based on observations of activity patterns (Bani et al., 2010; Vergnolle et al., 2013) and gas compositions (Allard et al., 2015). Acoustic survey by Bani et al. (2010) revealed that strong activity at Marum was preceded by increased acoustic events at both Marum and Benbow craters, while Vergnolle et al. (2013) suggested that a shared magma reservoir in which the roof slopes towards Marum could account for observed alternations between quiescence and Strombolian explosions at the two vents.

A number of observations suggest that magma ponding may occur at very shallow depths. The results of a magnetic survey (McCall et al., 1970) show the upper surface of an anomalous source body beneath the caldera at c. 300 m above sea level (~1 km below the surface), suggesting a perched magma chamber beneath the active cones. Allard

**Fig. 1.** a) Simplified structural map of Vanuatu after Greene et al. (1988), showing subduction front, major fracture zones, and the D'Entrecasteaux Ridge (DER), a subducting aseismic ridge which impinges on the arc near Ambrym. Ambrym island is marked by a black star. Inset shows the location of Vanuatu in the SW Pacific. PNG = Papua New Guinea. b) Geomorphological map of Ambrym showing the major features: caldera scarp, intracaldera cones, E–W-aligned flank fissures, coastal tuff rings, and N–S lineation of pre-shield peaks (Tuvio, Vetlam and Dalahum)—overlain on NASA satellite image. Marum cone, in the eastern part of the caldera, is the source of the samples examined in this study.

et al. (2015) report a cluster of melt inclusion entrapment pressures around  $130 \pm 20$  MPa (~4–5 km) based on dissolved volatile contents. A study of very long period tremor from July to November 2000 (Legrand et al., 2005) demonstrated the existence of two distinct tremor sources, associated with the western (basaltic) and eastern (trachyandesitic) intracaldera vents respectively. The tremor source associated with current intracaldera basaltic activity is located c. 3.7 km below the western part of the caldera floor, and the eastern source is c. 3.5 km below the eastern part of the caldera floor. Assuming a uniform density of  $2300 \text{ kg m}^{-3}$  to reflect the relatively low-density caldera infill of rumbly lavas and pyroclastic material (McCall et al., 1970) this translates to a pressure of 83 MPa for the basaltic region and 79 MPa for the trachyandesitic region.

At deeper levels, U.S. Geological Survey earthquake data for the period 1975–2013 show two major clusters of earthquakes, between 10 and 35 km and 170–210 km depth below Ambrym (Fig. 3a).

Blot (1981) suggested that the ‘deep root’ of Ambrym may be located at 150–200 km depth and slightly to the north of the island, based on apparent correlation of earthquakes with increased eruptive activity. Blot (1981) noted that delay times between deep earthquakes and eruptions clustered around 200 days, perhaps related to explosive or gas-rich events, and 315 days, perhaps related to magma ascent and lava flows—adding that paroxysmal activity often occurred on a time-scale of months following the beginning of an active phase with increased gas output. These observations indicate that deep seismic events are associated with magma release, and that volatile components appear to separate and precede the main body of magma to the surface.

Examination of seismic locations at shallower levels (0–60 km) reveals a series of apparent seismic gaps which may correspond to melt-rich zones, located at 50–35, 29–25, 21–12, and 10–0 km (Fig. 3b).

Crustal thickness for the central segment of the Vanuatu arc (from Malekula to Efate) has been estimated as  $27 \pm 2$  km on the trenchward side of the arc (Coudert et al., 1984). A gravity survey by McCall et al. (1970) found a gravity gradient across Ambrym island, indicating thicker crust, or lower-density crust and upper mantle, towards the west. McCall et al. (1970) suggested that the island may straddle a boundary between a lower-density (e.g. andesitic) lithology to the west and a higher-density (e.g. basaltic) lithology to the east. Translation of gravity anomalies into crustal thicknesses indicates a depth for the crust/mantle boundary of 20.8 km on the eastern side of the island and 24.8 km on the western side. These estimates suggest that the seismic gap around 29–25 km depth most likely reflects a structural control on the location of magma at this level.

Picard et al. (1995) calculated segregation depths of Ambrym source magmas by plotting sample compositions on the Ol–Jd + CaTs–Qz molecular normative projection (Jaques and Green, 1980; Falloon and Green, 1988; Falloon et al., 1988), which indicate that the most primitive basalts of Ambrym (Tuvio–Vetlam–Dalahum) originated from 45 to 60 km depth (1.5–2 GPa); and the basal shield and post-caldera magmas segregated at depths of 30–45 km (1–1.5 GPa). These depths approximately coincide with the lowermost potential magma storage region identified in Fig. 3b, at 50–35 km depth.

These studies provide broad constraints on the configuration of the magma system, from a ‘deep root’ at 150–200 km (Blot, 1981), to magma separation at 60–30 km (Picard et al., 1995), and staged melt zones from ~35–0 km.

### 3. Materials and methods

The selected samples are scoria and reticulite collected from the rim of Marum crater following elevated lava lake activity in 2005 and 2007.

The 2005 sample is a c. 40% vesicular scoria, 15–20% porphyritic and dark grey to black in colour. The phenocryst phases are plagioclase (10–18%), clinopyroxene (~3%), olivine (0.5–2%) and Fe–Ti oxides (<1%), and mainly occur in glomerocrystic clots. Clinopyroxene and

olivine also occur as individual rounded or euhedral crystals. The matrix varies from pale brown glass (c. 50–80%) to microcrystalline or cryptocrystalline groundmass (c. 5–35%).

The 2007 sample is a c. 85% vesicular reticulite, found interspersed with fragments of Pelé’s hair on the crater rim. Phenocrysts of up to 1 mm of plagioclase (~5%) and clinopyroxene (~2%) occur in clusters of 1–2 mm diameter, and both, particularly clinopyroxene, often display rounded outlines. The largest plagioclase phenocrysts display many rounded or convolute zones. Clusters of up to 500  $\mu\text{m}$  in diameter of smaller plagioclase crystals also occur. Clinopyroxene phenocrysts (up to 1200  $\mu\text{m}$ ) are euhedral to heavily rounded, while olivine phenocrysts (up to 600  $\mu\text{m}$ ) are euhedral to rounded and occur in clusters of up to 1 mm. The matrix consists of pale brown glass.

#### 3.1.1. X-Ray fluorescence

Major elements were analysed by X-ray fluorescence on a Bruker AXS S4 Pioneer spectrometer in the Geotechnical Microanalysis Laboratory at the University of East Anglia, using glass beads. Six repeats of each sample were performed to confirm repeatability of the data.

#### 3.1.2. EMPA analytical procedure

Mineral, glass and melt inclusion compositions were analysed on a Cameca-SX100 electron microprobe at the University of Cambridge. The accelerating voltage was 15 keV for all analyses. Major elements in minerals were analysed with a 10 nA beam current and minor elements with a 100 nA beam current, except for clinopyroxene, for which a 60 nA current was used.

Beam sizes used were 10  $\mu\text{m}$  for glass and 0  $\mu\text{m}$  (nominal; actual size of c. 3  $\mu\text{m}$ ) for plagioclase, clinopyroxene, olivine, and spinel. Counting times of 20–30 s were used, with longer counting times of 60 s for Cl, S, P and 180 s for F in matrix glass and melt inclusions. Analytical error is <3% ( $2\sigma$ ) for all elements.

#### 3.1.3. Thermobarometry

Several models were used to calculate temperature and pressure using compositions of minerals and/or melt.

##### 3.1.3.1. Clinopyroxene thermobarometry

Two sets of clinopyroxene–melt thermobarometers were applied in order to check the consistency of the results. The temperature and pressure models of Putirka et al. (2003) were chosen due to having the highest precision ( $R^2 = 0.96$  and  $0.97$  respectively) and lowest error (33 °C and 170 MPa respectively) of currently available models. Eqs. 30 and 33 of Putirka (2008), with  $R^2$  values of 0.83 and 0.92 respectively, and errors of 360 MPa and 45 °C respectively, were also applied for purposes of comparison.

Both barometers are based on the large change in molar volume involved in jadeite formation (i.e., the large partial molar volumes of Na and Al in liquid compared to the small molar volume of jadeite), while the thermometers are based on the temperature-sensitivity of the jadeite–diopside/hedenbergite exchange between clinopyroxene and coexisting melt.

A clinopyroxene-only barometer and thermometer (Eqs. 32a and 32d of Putirka, 2008) with errors of 310 MPa and 58 °C respectively, were also applied as an independent test of results from the clinopyroxene–melt calculations.

The crystal–liquid models used incorporate two tests for equilibrium. The first compares the clinopyroxene–liquid Fe–Mg partition coefficient ( $K_D^{\text{Fe–Mg}}$ ) to the experimentally-determined equilibrium value of  $0.27 \pm 0.03$  (Putirka, 2008). The second compares predicted equilibrium clinopyroxene compositions (constrained from experiments) with measured values for pyroxene components EnFs, DiHd, and CaTs, calculated using a normative procedure of Putirka et al. (2003).

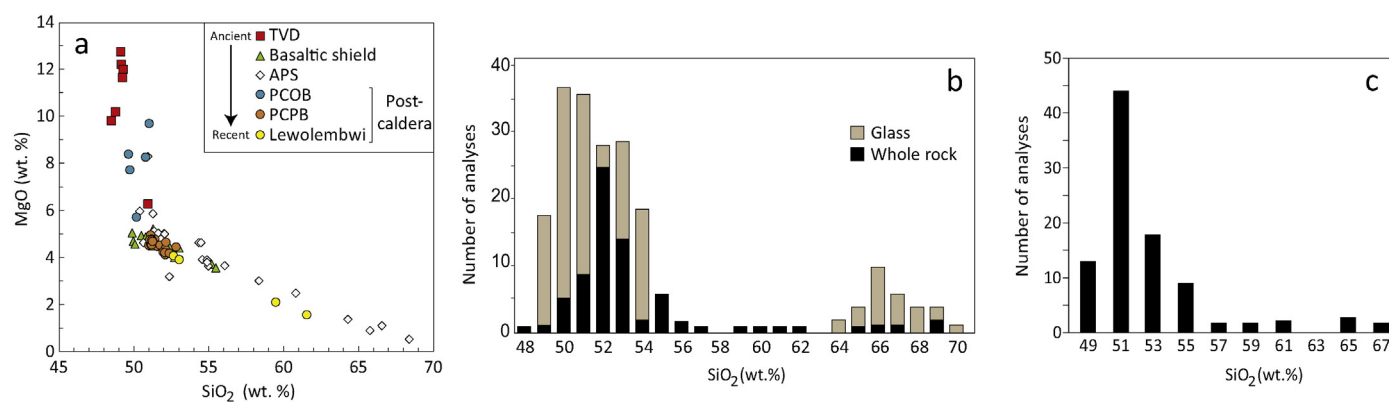


**Fig. 2.** Overview of Ambrym geochemistry, using data from Picard et al. (1995). a) MgO vs. SiO<sub>2</sub> for the four major volcanic phases of Ambrym, showing progression from most primitive (TVD), to the predominant basaltic composition clustering around 50–53 wt.% SiO<sub>2</sub>, with excursions to higher-silica occurring in the Ambrym Pyroclastic Series (APS) and recent trachyandesite in the eastern part of the caldera. TVD = Tuvio–Vetlam–Dalalum edifices. APS = Ambrym Pyroclastic Series (tuff cone). PCOB = post-caldera olivine basalts. PCPB = post-caldera plagioclase basalts. Lewolembwi samples derive from in the eastern part of the caldera. There is significant overlap between shield basalt, PCPB and APS around the change in slope. b) Histogram of 137 glass analyses from vitric clasts of the APS and 68 whole rock analyses from the entire volcano; class interval 1%. c) Histogram of 96 whole rock analyses from entire volcano, Class interval = 2%, label represents median value (e.g. 49 represents 48–50 wt.%).

### 3.1.3.2. Plagioclase-melt thermobarometry

The plagioclase thermometer Eq. 24a of Putirka (2008) is used here as it shows higher precision ( $R^2 = 0.93$ ) and lower error ( $\pm 36$  °C) than previous models. Putirka (2008) also presents a plagioclase-liquid barometer (Eq. 25a), which is recommended only for compositions closely similar to specific datasets for which it works well. The test composition to which recent Ambrym basalts fall closest is the high-K basalt of Meen (1990), for which the model does not perform with great precision, although the results do bracket the real values. For example, experimental samples equilibrated at 1 GPa give results of 0.5–1.4 GPa, and samples

equilibrated at 1.5 GPa give results of 0.8–1.6 GPa. Pressure estimates from this barometer are thus regarded with caution, but are included in the absence of more precise methods for estimation of plagioclase crystallisation depths.

Both the plagioclase thermometer and barometer require an initial pressure estimate, which has a significant effect on calculated values of pressure and temperature. An estimate derived from clinopyroxene barometry has been used in this case.

The albite–anorthite exchange coefficient,  $K_D^{Ab-An}$ , is used as a test for equilibrium, and has been experimentally determined to be  $0.27 \pm 0.11$  for liquids  $> 1050$  °C (Putirka, 2008).

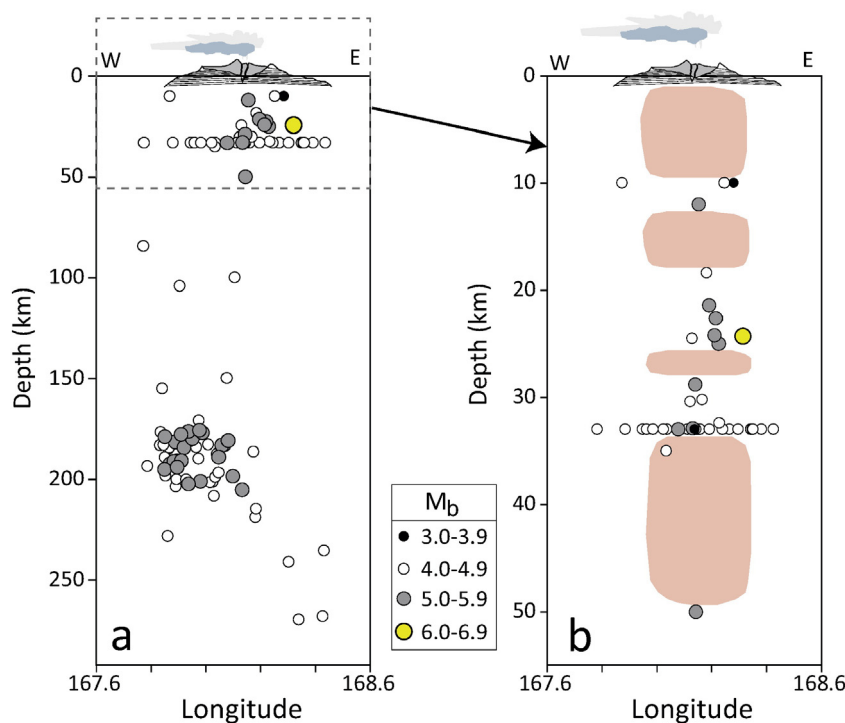


**Fig. 3.** Earthquakes below Ambrym during the period 1975–2013, displayed on an east–west transect. Earthquakes located by the U.S. Geological Survey National Earthquake Information Center. Magnitude is in  $M_b$ ; some values have been converted from  $M_w$  or  $M_s$  following Scordilis (2006). Earthquake locations are located by longitude; the illustration of the volcanic edifice is also matched to actual longitudinal position. a) Data to 300 km depth. Ambrym volcano is shown with vertical exaggeration of  $\times 6$  compared to the sub-sea-level depth scale. The dashed box outlines the area shown in panel b. b) Shallow earthquake data (0–55 km), based on which inferred hot zones where magma storage may occur are marked by pink shaded areas. Ambrym volcano is shown to scale with sub-sea-level depths.

### 3.1.3.3. Olivine–melt thermometry

Olivine–melt thermometry calculations were performed using Eq. 22 of Putirka (2008), which shows the best precision and lowest error ( $\pm 29^\circ\text{C}$ ) of a range of models evaluated in that study.

Equilibrium is tested by comparison to values of  $K_D^{\text{Fe-Mg}}$  derived from experimental data. A value of  $0.30 \pm 0.03$  (Roeder and Emslie, 1970) is widely used and remains regularly cited in the literature (e.g., Danyushevsky and Plechov, 2011; Marsh, 2013; Sides et al., 2014). Putirka (2008) tested this value using data from 1504 experiments, which returned a value of  $0.30 \pm 0.05$ , slightly extending the range of the classic Roeder and Emslie (1970) value.

## 4. Results

### 4.1. Whole rock, glass and melt inclusion compositions

Whole rock, glass and melt inclusion compositions are given in Table 1. Whole rock compositions plot in the basalt field, while melt inclusions from both samples are mainly basaltic andesite to basaltic trachyandesite, and matrix glasses plot in the basaltic trachyandesite field (Fig. 4).

#### 4.1.1. Petrography and mineral compositions

The analysed dataset for the 2005 scoria consists of 267 plagioclase analyses, 72 clinopyroxene analyses, 30 olivine analyses, 26 Fe–Ti oxide analyses and 23 glass analyses. The dataset for the 2007 reticulite consists of 9 plagioclase analyses, 4 clinopyroxene analyses, 6 olivine analyses, 7 Fe–Ti oxide analyses and 3 glass analyses.

**4.1.1.1. Plagioclase.** Plagioclase occurs primarily as glomerocrysts, labelled here as ‘coarse’ and ‘fine’ types. The ‘coarse’ variant are the largest and most texturally complex phenocryst phase, up to c. 1000–3000  $\mu\text{m}$  in diameter, with crystals of c. 250–1500  $\mu\text{m}$  along the long axis, either jumbled, lath-shaped crystals with blurred twinning and recrystallised grain boundaries, or blocky, rounded crystals with conspicuous fritted cores or zones (Fig. 5a, b); these blocky glomerocrysts often include large ragged or rounded clinopyroxene crystals (Fig. 5b). ‘Fine’ glomerocrysts are 300–800  $\mu\text{m}$  in diameter, comprised of crystals of c. 100–400  $\mu\text{m}$  along the long axis, typically blocky and markedly more distinct in outline than those in the coarse glomerocrysts. The euhedral shape and lack of rounding or fritting indicate that these crystals grew in equilibrium with the matrix glass. Finally, scattered microphenocrysts of 50–200  $\mu\text{m}$  are found singly in the matrix glass, either blocky and rectangular (which may be related to fine clot crystals), or ragged and irregularly shaped. Where present, groundmass crystals are anhedral and angular, c. 5–30  $\mu\text{m}$  in size, and interlocking with clinopyroxene, olivine, Fe–Ti oxides and interstitial glass. All of these plagioclase types occur in

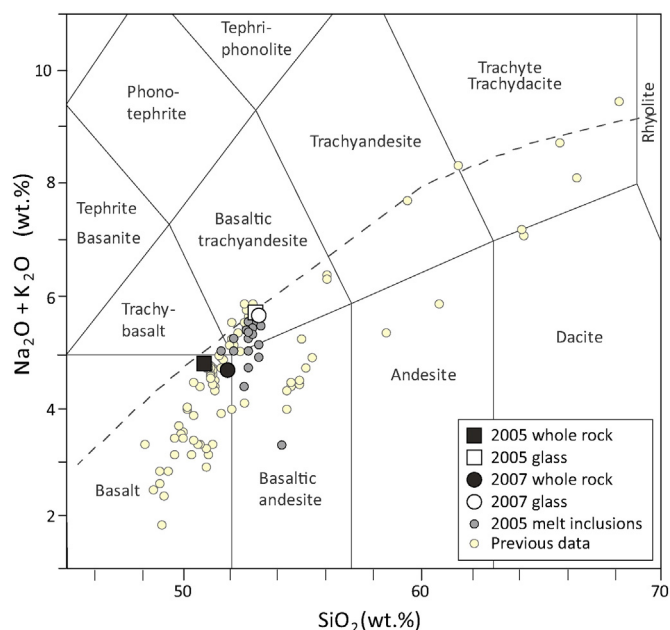


Fig. 4. Total alkalis versus silica (TAS) diagram (Le Bas et al., 1986) showing bulk rock, glass and melt inclusion compositions from 2005 and 2007 scoria. Previously published data is included for reference (Picard et al., 1995; Robin et al., 1993; Gorton, 1977).

the 2005 scoria, but only coarse glomerocrysts and rare groundmass microlites occur in the 2007 reticulite.

In the 2005 scoria, anorthite contents range from  $An_{89-46}$ , with significant compositional overlap between crystal types (Fig. 6). Phenocrysts in coarse glomerocrysts have cores of  $An_{89-75}$ , with rims of  $An_{71-67}$ . These crystals display normal zoning, with both stepped and gradual profiles which are occasionally slightly oscillatory. The anorthite contents of fine glomerocrysts are  $An_{81-68}$ . Weak normal zoning is seen in the fine glomerocryst plagioclase, with cores of  $An_{81-71}$  and rims of  $An_{80-68}$ , mainly towards the lower end of the range. Microphenocrysts show a compositional range of  $An_{81-56}$ , including a distinct population of blocky to elongate laths of  $\sim 50\text{--}70\ \mu\text{m}$  with compositions in the range  $An_{68-56}$ . Zoning is generally normal but is asymmetrical across some crystals, likely a function of crystallographic orientation or fragmentation of larger crystals. Apparent groundmass crystals cover a wide range of compositions from  $An_{79-46}$ , although the bulk of the analyses cluster around  $An_{58-46}$  (Fig. 6). Higher-anorthite crystals in this group may represent phenocryst or microphenocryst fragments.

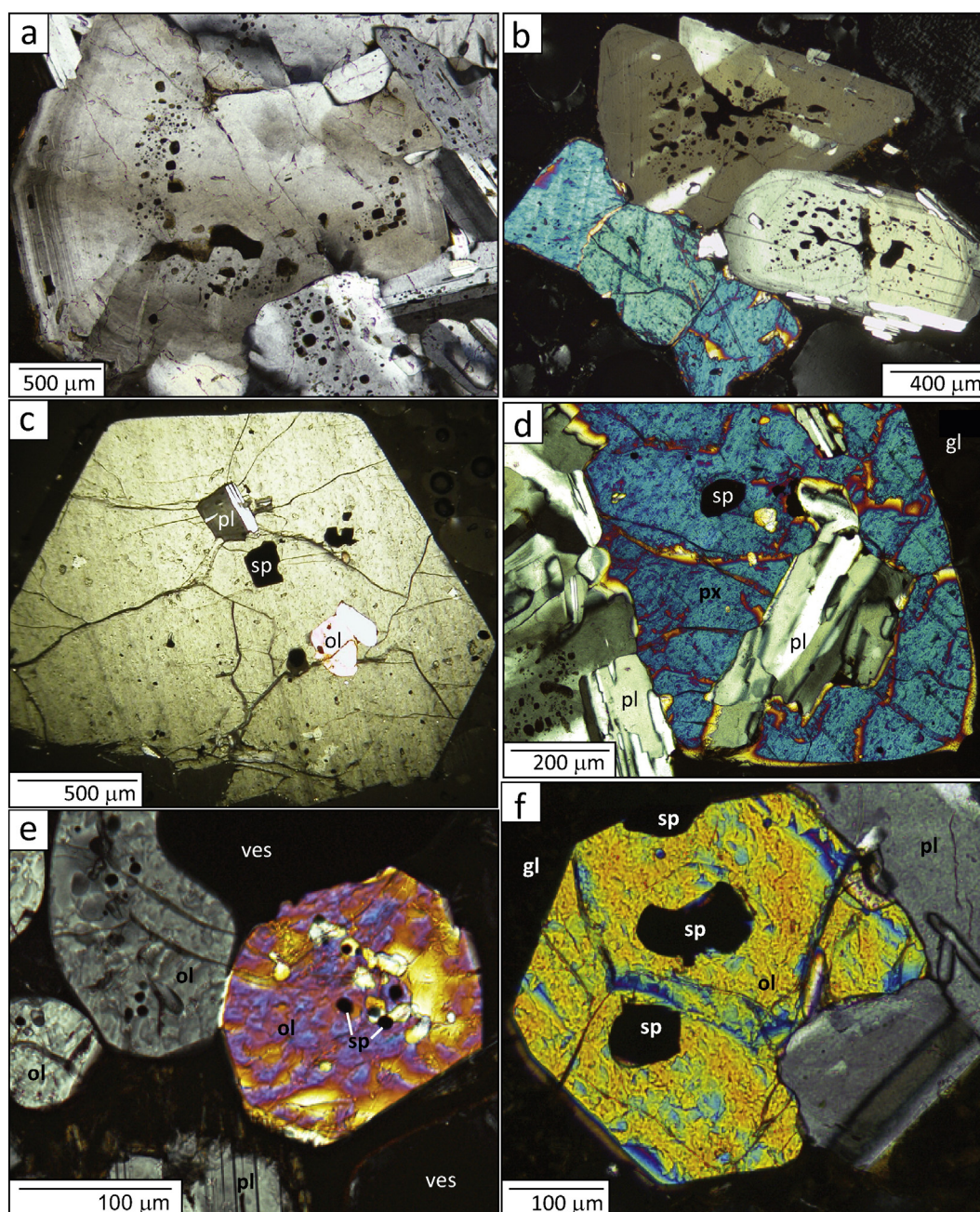
In the 2007 reticulite, anorthite contents range from  $An_{83-64}$ . The number of plagioclase analyses is much lower for this sample;  $n = 9$ ,

Table 1

Bulk rock, matrix glass and representative olivine- and clinopyroxene-hosted melt inclusion compositions (i.e., real compositions which fall close to the mean).

Sample	2005				2007		
	WR	Glass	OI MI	Cpx MI	WR	Glass	MI
n	6	23	3	3	6	5	3
SiO <sub>2</sub>	50.79	52.55 (0.33)	51.29 (0.54)	51.70 (0.24)	51.45	52.40 (0.31)	51.49 (0.07)
TiO <sub>2</sub>	0.91	1.12 (0.05)	1.03 (0.05)	1.02 (0.05)	0.96	1.11 (0.07)	0.61 (0.03)
Al <sub>2</sub> O <sub>3</sub>	16.81	14.53 (0.18)	14.76 (0.23)	14.37 (0.06)	15.56	14.28 (0.20)	14.00 (0.17)
FeO	10.15	11.78 (0.48)	12.26 (0.29)	12.04 (0.45)	10.49	11.54 (0.26)	12.62 (0.17)
MnO	0.20	0.24 (0.03)	0.26 (0.02)	0.24 (0.01)	0.20	0.23 (0.02)	0.28 (0.03)
MgO	4.50	4.41 (0.51)	4.34 (0.14)	4.49 (0.08)	4.27	4.56 (0.11)	5.04 (0.04)
CaO	9.02	8.25 (0.55)	8.51 (0.18)	8.40 (0.03)	8.44	8.49 (0.20)	9.74 (0.14)
Na <sub>2</sub> O	2.93	3.24 (0.12)	3.24 (0.02)	3.12 (0.08)	2.79	3.30 (0.03)	2.78 (0.03)
K <sub>2</sub> O	1.97	2.47 (0.15)	2.21 (0.01)	2.21 (0.01)	1.97	2.40 (0.09)	1.45 (0.03)
P <sub>2</sub> O <sub>5</sub>	0.33	0.44 (0.02)	0.42 (0.00)	0.42 (0.02)	0.34	0.43 (0.02)	0.30 (0.01)
LOI	−0.46	–	–	–	n.d.	–	–
Total	97.14	99.12 (0.48)	98.51 (0.40)	98.18 (0.59)	97.62	98.85 (0.40)	98.60 (0.24)

For melt inclusions, n represents number of analyses on a single inclusion. Figures in parentheses = one standard deviation. All iron is reported as FeO<sub>Total</sub>. Whole rock totals are slightly low due to recalculation of Fe from Fe<sub>2</sub>O<sub>3</sub>.



**Fig. 5.** Representative photomicrographs (crossed polars) of phenocryst types in 2005 basaltic scoria. a) Rounded, blocky coarse glomerocrystic plagioclase with heavily fritted zone and embayed concentric zoning. b) Rounded, blocky coarse glomerocryst plagioclase with sieve-textured cores, and large rounded to ragged clinopyroxene phenocrysts. c) Large euhedral clinopyroxene with plagioclase, Fe–Ti oxide and olivine inclusions. d) Rounded clinopyroxene attached to coarse plagioclase glomerocryst, with plagioclase and Fe–Ti oxide inclusions. e) Rounded olivine phenocrysts with abundant Fe–Ti oxide inclusions. f) Large euhedral olivine (ol) with Fe–Ti oxide (sp) inclusions, associated with plagioclase glomerocryst (pl).

as compared to  $n = 267$  for the 2005 scoria. Phenocrysts display compositions of  $An_{83(\text{core})-76(\text{rim})}$ , while plagioclase inclusions in clinopyroxene or olivine show compositions of  $An_{68-64}$ .

**4.1.1.2. Clinopyroxene.** In the 2005 scoria, clinopyroxene occurs as euhedral phenocrysts up to  $1500 \mu\text{m}$  (Fig. 5c) or blocky to ragged phenocrysts of c.  $200\text{--}700 \mu\text{m}$ ; a rounded or ragged glomerocryst phase of  $\sim 200\text{--}800 \mu\text{m}$  (Fig. 5d); rare clusters of subhedral crystals of  $300\text{--}900 \mu\text{m}$ ; and ragged or rounded subhedral microphenocrysts ( $\sim 100\text{--}300 \mu\text{m}$ ). Groundmass clinopyroxene, where present, occurs as diamond-shaped or angular anhedral crystals of  $\sim 5\text{--}20 \mu\text{m}$ , interlocking with other groundmass phases. The large euhedral

phenocrysts contain frequent inclusions of Fe–Ti oxide, occasional plagioclase, and rare olivine.

Clinopyroxene in the 2007 reticulite occurs as a large, rounded glomerocrystic phase ( $500\text{--}1500 \mu\text{m}$ ), angular or euhedral phenocrysts of up to  $1000 \mu\text{m}$ , and rare clinopyroxene-only glomerocrysts of up to  $1000 \mu\text{m}$  size, with euhedral to rounded constituent crystals of  $50\text{--}200 \mu\text{m}$ . All types occur in conjunction with rounded, stubby Fe–Ti oxide phenocrysts of  $50\text{--}250 \mu\text{m}$ , and Fe–Ti oxide inclusions of  $10\text{--}50 \mu\text{m}$ .

In both samples, phenocrystic and glomerocrystic clinopyroxene compositions cluster in the augite field, around  $\sim En_{42-44}Wo_{41-44}Fs_{14-15}$  (Table 2; Fig. 6b). Concentric growth zonation can be seen in some of the large euhedral clinopyroxenes, which electron microprobe analysis

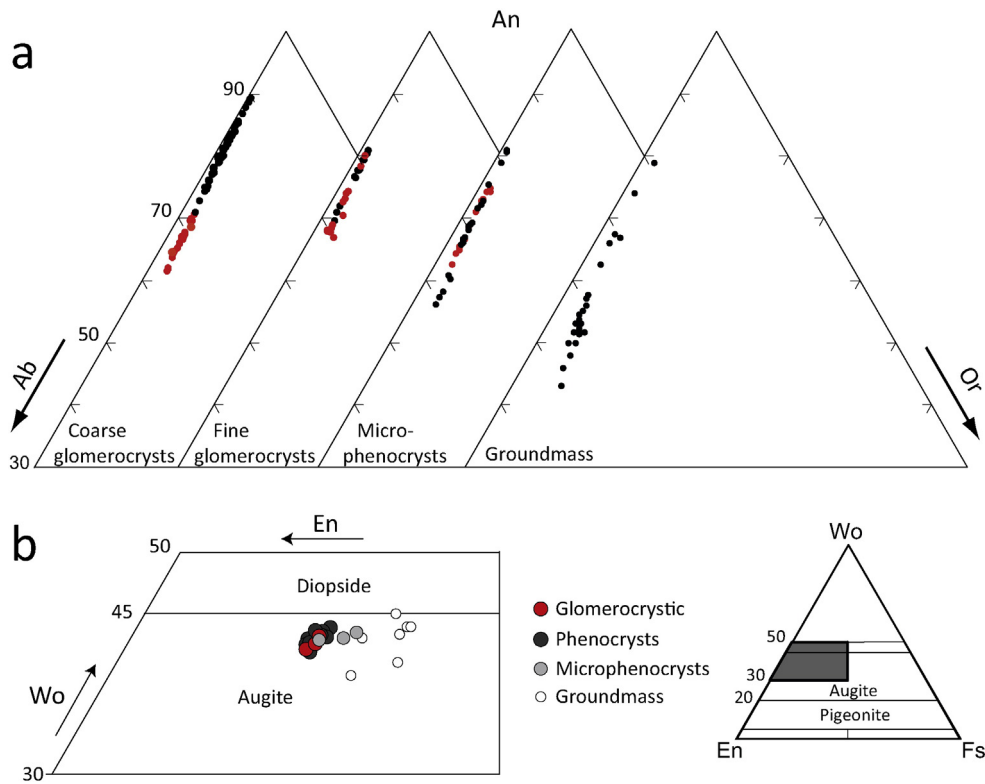


**Fig. 6.** a) Composition of all analysed plagioclase datapoints, in both the 2005 and 2007 samples. Only coarse glomerocrystic plagioclase is present in the 2007 sample. Plagioclase compositions range from An<sub>89</sub> to An<sub>46</sub>. Black = core, red = rim; except for groundmass analyses which are not symbolically differentiated. b) Clinopyroxene compositions (n = 35), showing both glomerocrystic and individual phenocrysts from both the 2005 and the 2007 samples tightly clustered in the augite field, with microphenocrysts and groundmass (present in the 2005 samples only) showing scatter towards more Fe-rich compositions. (For interpretation of the references to colour in this figure legend, the reader is referred to the web version of this article.)

shows to be minor oscillatory zoning, within the compositional range given above. Sector zoning is seen in euhedral and rounded subhedral phenocrysts. Microphenocrysts and groundmass crystals show a wider compositional spread than the phenocrysts (over the range En<sub>26–42</sub>-Wo<sub>38–46</sub>Fs<sub>18–31</sub>), with higher Fe and Al contents, and lower MgO (Fig. 6b).

**4.1.1.3. Olivine.** In the 2005 scoria, olivine primarily occurs as rounded or euhedral to subhedral phenocrysts of up to 400 μm with Fe-Ti oxide inclusions, primarily in glomerocrysts (Fig. 5e,f). Occasional isolated rounded grains and angular crystals are also present. In the groundmass, olivine occurs as subhedral to euhedral crystals of 10–30 μm. No zoning is present in any of these crystal types.

In the 2007 reticulite, olivine occurs as single or clustered rounded-to-euhedral phenocrysts of 100–600 μm, and angular or rounded groundmass crystals (10–20 μm).

Olivine in the 2005 scoria has a homogeneous composition of Fo<sub>74.9 ± 0.4</sub> despite variations in size and morphology, while the 2007 reticulite contains marginally more forsteritic olivine (An<sub>75.5 ± 0.3</sub>), again effectively homogeneous in all crystal types, from large clot phenocrysts to rare groundmass microlites (Table 2).

**4.1.1.4. Matrix glass and melt inclusions.** The matrix glass is basaltic trachyandesitic and is of identical composition in samples from 2005 and 2007 (Table 1). Melt inclusions (olivine- and clinopyroxene-

**Table 2**  
Representative mineral compositions, i.e., real compositions which fall close to the mean.

	2005 scoria					2007 reticulite											
	Plagioclase					Cpx		Ol	Fe-ox	Plagioclase					Cpx	Ol	Fe-ox
	CGC	CGR	FGC	FGR	Gm	Ph	Mp	All	All	CGC	CGR	Ph	Ph	All	Ph	Ph	All
SiO <sub>2</sub>	45.21	50.05	46.68	50.4	53.87	50.85	46.77	38.76	0.15	47.37	50.61	50.54	38.83	0.14			
TiO <sub>2</sub>	0.01	0.03	0.03	0.04	0.08	0.50	1.30	0.03	4.36	0.02	0.03	0.56	0.01	4.70			
Al <sub>2</sub> O <sub>3</sub>	32.86	29.26	31.33	29.49	26.72	3.43	5.99	0.04	6.04	32.25	29.37	3.92	0.04	5.89			
FeO <sup>a</sup>	1.13	1.22	1.27	1.35	2.05	9.17	11.64	22.86	78.32	1.03	1.08	8.95	22.10	77.11			
MnO	0.01	0.01	0.00	0.00	0.03	0.28	0.26	0.47	0.35	0.01	0	0.21	0.48	0.32			
MgO	0.08	0.15	0.13	0.16	0.39	14.95	11.81	38.35	4.76	0.12	0.16	14.74	38.44	4.70			
CaO	17.66	13.94	15.69	13.52	10.92	19.93	20.34	0.33	–	16.83	13.95	20.74	0.31	–			
Na <sub>2</sub> O	1.12	3.11	2.12	3.21	4.88	0.35	0.44	0.02	–	1.93	3.36	0.36	0.01	–			
K <sub>2</sub> O	0.09	0.31	0.2	0.38	0.69	0.00	0.08	0.01	–	0.16	0.36	0.00	–	–			
Cr <sub>2</sub> O <sub>3</sub>	–	–	–	–	–	–	–	–	0.40	–	–	–	–	0.49			
Total	98.17	98.13	98.49	98.57	99.61	99.49	98.63	100.97	94.56	99.84	99.06	100.07	100.4	93.37			
<sup>a</sup>	89	70	79	68	53	74	64	75		82	68	75	75				

CGC = coarse glomerocryst core, CGR = coarse glomerocryst rim, FGC = fine glomerocryst core, FGR = fine glomerocryst rim, gm = groundmass, ph = phenocryst, mp = microphenocryst, Fe-ox = Fe-Ti oxide.

<sup>a</sup> Denotes anorthite mol%, Mg# or forsterite mol%.

hosted) in both samples are of basaltic trachyandesite to basaltic andesite composition and lie between the whole rock and matrix glass compositions (Fig. 4).

#### 4.1.2. Thermobarometry results

Nominal melts used for mineral–melt equilibria were whole rock and matrix glass. Whole rock, melt inclusion and glass compositions lie along whole-rock trends for the volcanic succession (Fig. 4), which suggests that they are suitable nominal liquids. The mineral–liquid pairs chosen for testing are those which satisfy the tests for equilibrium detailed in Section 3.1.3.

Mineral–melt pairs have been investigated at 0.6 and 1.3 wt.% H<sub>2</sub>O, based on recent measurements of dissolved H<sub>2</sub>O contents of 0.6–1.3 wt.% in olivine-hosted melt inclusions at Ambrym (Allard et al., 2015).

Pressure and temperature results cited below represent means of results from multiple mineral–melt pairs, with one standard deviation as the error. Results for clinopyroxene- and plagioclase–melt equilibria show a marked scatter at either end of their ranges, which also correspond to the  $K_D$  values furthest from equilibrium; results which fall outside the range of  $\pm 1\sigma$  for two or more variables have thus been removed to exclude unreliable outliers.

**4.1.2.1. Oxygen fugacity.** An olivine–spinel–pyroxene oxythermometer based on the thermodynamic models of Sack & Ghiorso (1989, 1991a, b, 1994a,b,c) was used to estimate  $fO_2$ . This method uses empirical thermodynamic constraints on Fe–Mg exchange between adjacent olivine and spinel crystals to calculate temperature using experimentally-derived  $K_D^{Fe-Mg}$  values, and this, combined with a pyroxene composition, returns an  $fO_2$  estimate for a given pressure. The calculator is nominally designed for use with orthopyroxene but using clinopyroxene should have only a minor effect on the results, well within the uncertainty of the calculations (Ghiorso, 2010, pers. comm.). The model is available as a web applet on the Computational Thermodynamics Server ([http://ctserver.ofm-research.org/Olv\\_Spn\\_Opx/index.php](http://ctserver.ofm-research.org/Olv_Spn_Opx/index.php)).

Calculations were made using phenocrystic olivine and spinel, which are compositionally invariant within both samples studied, and phenocrystic clinopyroxene, which shows only minor compositional variance. Close spatial association of these compositional types, particularly occurrence of all three phases in glomerocrysts, indicates a cogenetic relationship and likelihood of equilibrium. Microphenocrystic or groundmass clinopyroxenes are excluded as they appear from Na–Al contents to represent disequilibrium (rapid) growth. The  $T$ - $fO_2$  calculated then represents the conditions of crystallisation of phenocrystic olivine, pyroxene, and spinel. Results from the olivine–spinel–pyroxene oxythermometer are listed in Table 3. The associated error is  $\pm 0.5$  log units (Wood, 1991).

**4.1.2.2. Clinopyroxene–melt and clinopyroxene–only thermobarometry.** Results given here include only those pairs which have  $K_D^{Fe-Mg}$  values within the equilibrium range of  $0.27 \pm 0.03$ . In general, phenocryst/whole rock pairs in both samples satisfy the  $K_D^{Fe-Mg}$  test for equilibrium but groundmass/glass pairs (2005 scoria only) do not (Fig. 7a). Disequilibrium  $K_D^{Fe-Mg}$  values for groundmass/glass pairs suggest that groundmass crystals represent rapid disequilibrium growth, which entails high Al and Na uptake; high Al and Na contents are observed in the groundmass crystals. In some cases, this may be a result of fluorescence of adjacent

glass, evidence of which can be seen in elevated K<sub>2</sub>O contents—up to 0.6 wt.% in some groundmass clinopyroxene analyses. A graph of observed versus predicted values for the DiHd component shows almost all groundmass/glass pairs from 2005 straddling the 1:1 line, with phenocryst/whole rock pairs in both samples offset but within 5% of the line (Fig. 7b). These results indicate that the component test alone is not sufficient to demonstrate equilibrium for the purposes of thermobarometry, as pressure estimates from groundmass–glass pairs are much higher than phenocryst–WR pairs, and are clearly spurious given the late-stage nature of groundmass crystallisation.

For the 2005 scoria, average barometry results for phenocrysts, taking three models (the most precise and accurate, Putirka et al., 2003; a model based on different exchange equilibria, Putirka, 2008; and an independent check on both of these, clinopyroxene-only model 32d) into account, range from 390 to 450 MPa (c. 15–17 km depth) (Tables 4 & 5; Fig. 8). Temperatures from mineral–melt thermometry are c. 1100–1140 °C, while clinopyroxene-only thermometers gives results of c. 1170 °C.

For the 2007 samples, average barometry results from all three models range from 390 to 490 MPa (c. 15–18 km depth) and 1100–1150 °C (Tables 4 & 5; Fig. 8). The clinopyroxene-only thermometer gives a higher temperature of 1170 °C.

**4.1.2.3. Olivine thermometry.** Results from olivine thermometry provide an independent check on the reliability of results from clinopyroxene, as these phases appear texturally to have crystallised at or near the same time.

Olivine phenocrysts display both equilibrium and resorption morphologies. Phenocrystic olivine compositions are homogeneous (~F<sub>075</sub>), and identical to groundmass olivine compositions, which suggests crystallisation from an identical host melt.  $K_D^{Fe-Mg}$  values were calculated at  $Fe^{2+}/\Sigma Fe$  corresponding to  $fO_2 \sim NNO + 1.2$ , via the method of Kress and Carmichael (1991). The resulting values are high (0.37–0.44; Table 6, Fig. 9) compared to the nominal equilibrium value ( $0.30 \pm 0.03$ ) of Roeder and Emslie (1970), and the updated value of  $0.30 \pm 0.05$  of Putirka (2008). Given the moderately high alkali content of the rocks and matrix glass (total alkalis of 4.9–5.8 wt.%), an adjustment of  $K_D^{Fe-Mg}$  for alkali content (Toplis, 2005) was applied to investigate whether adjusted  $K_D^{Fe-Mg}$  values more closely approach equilibrium. In addition, groundmass olivine must be in equilibrium with the matrix glass but returns non-equilibrium values according to Roeder and Emslie (1970) and Putirka (2008), suggesting that their  $K_D^{Fe-Mg}$  values do not reflect equilibrium for this melt composition. The Toplis (2005) adjustment shifts  $K_D^{Fe-Mg}$  values to 0.30 (Table 6). An alternative check using the method of Kushiro and Walter (1998), in which  $K_D^{Fe-Mg}$  values are adjusted for melt composition using NBO/T ratios, gives results in the range 0.29–0.30, which agree with those calculated using Toplis (2005) to within 0.01 (Table 6). Olivine–melt pairs are thus considered to represent equilibrium.

Temperature estimates were examined at 0.6 and 1.3 wt.% H<sub>2</sub>O, and pressures of 400 MPa for whole rock, based on mid-crustal storage conditions indicated by clinopyroxene barometry (~400 MPa), and a pressure of 100 MPa for glass, based on depths of very long period tremor sources (Legrand et al., 2005).

Results indicate temperatures of ~1090–1120 °C for 2005 scoria and ~1100–1110 °C for 2007 reticulate over the investigated range of 100–400 MPa and 0.6–1.3 wt.% H<sub>2</sub>O (Table 7).

**4.1.2.4. Plagioclase–melt thermobarometry.**  $K_D^{Ab-An}$  values suggest that plagioclase of An<sub>80–62</sub> is in equilibrium with the whole rock, while plagioclase of An<sub>72–51</sub> is in equilibrium with the matrix glass. Compositions in equilibrium with the whole rock are coarse glomerocryst rims, fine glomerocryst cores and rims, and microphenocrysts. Glomerocryst rims, microphenocrysts and groundmass compositions are in equilibrium with the matrix glass. Coarse glomerocryst cores are not in equilibrium with the whole rock, indicating an inherited/antecrystic phase

**Table 3**

$T$ - $fO_2$  calculations from the Sack & Ghiorso calculator over a range of pressures, for both samples.

P (MPa)	T (°C)	log $fO_2$	$\Delta NNO$
100	1140	−7.04	1.2
500	1170	−6.55	1.4
1000	1200	−5.98	1.5

$\Delta NNO$  is the value of  $fO_2$  relative to the nickel–nickel oxide (NNO) buffer as defined by Huebner and Sato (1970). Temperature results are rounded to three significant figures.

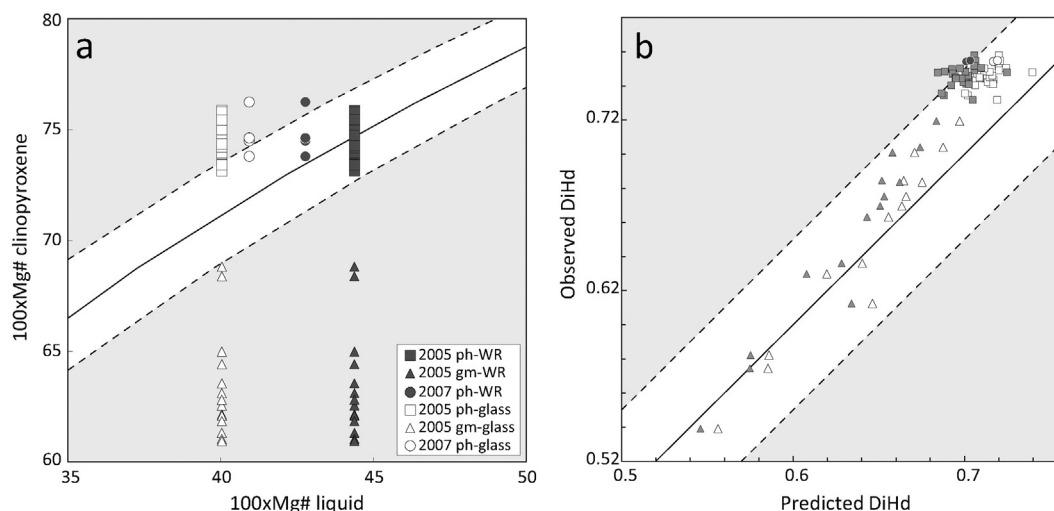


**Fig. 7.** Tests for equilibrium between clinopyroxene and nominal melts. a) Plot showing the equilibrium range for clinopyroxene and melt compositions, with equilibrium line  $K_D^{Fe-Mg} = 0.27$  (solid line)  $\pm 0.3$  (dashed lines). Whole rock compositions of 2005 and 2007 scoria give  $K_D^{Fe-Mg}$  values within the equilibrium range for phenocryst compositions, indicating that these crystal-liquid pairs are the best match for thermobarometry, whereas matrix glass and groundmass clinopyroxene compositions do not form any viable matches. b) Predicted vs. observed diopside-hedenbergite components. Symbols are the same as in Fig. 6a. This method indicates equilibrium where the  $K_D^{Fe-Mg}$  test does not, between the groundmass phase and both whole rock and glass. Petrographic considerations and unrealistically high P-T results for these crystal-liquid pairs indicate that the component diagram is a poor method for evaluation of equilibrium in this case.

which crystallised from a more mafic melt than the host rock. Plagioclase compositions form a continuum from most to least anorthitic with zoning or decreasing crystal size (Fig. 6a), suggesting continuous evolution with magma ascent and crystallisation.

Results of plagioclase-melt thermobarometry are strongly influenced by estimated water content of the melt, which significantly reduces both temperature and pressure estimates with increasing H<sub>2</sub>O content. Results have been tested over a range of dissolved water content for Ambrym of 0.6–1.3 wt.% H<sub>2</sub>O, as recently measured by Allard et al. (2015).

Averaged plagioclase thermobarometry results are listed in Table 8. The results indicate two major P-T regions (Fig. 10). At 0.6 wt.% H<sub>2</sub>O, these cover a range of 1170–1180 °C and 640–770 MPa for plagioclase in equilibrium with 2005 whole rock (An<sub>63–80</sub>), and 1140 °C and 360–510 MPa for plagioclase in equilibrium with 2005 matrix glass (An<sub>56–72</sub>). At 1.3 wt.% H<sub>2</sub>O, P-T estimates are lowered to 1140–1150 °C and 570–680 MPa in equilibrium with whole rock, and 1110–1120 °C and 280–440 MPa in equilibrium with matrix glass (Fig. 10a). Results

for the 2007 reticulite suggest crystallisation of plagioclase at slightly lower temperature and pressure than the 2005 phenocrysts, covering a range at 0.6 wt.% H<sub>2</sub>O of 1160–1170 °C and 440–590 MPa in equilibrium with whole rock, and 1140 °C and 360–410 MPa in equilibrium with glass (Fig. 10b). At 1.3 wt.% H<sub>2</sub>O, P-T estimates are 1130–1140 °C and 360–500 MPa for whole rock, and 1110–1120 °C and 280–330 MPa for glass.

Given the variable accuracy of the plagioclase barometer (see Materials and methods section), these results provide only a rough estimate of pressure, although the significant overlap of pressure estimates for lower-anorthite plagioclase phenocrysts in equilibrium with glass (~300–420 MPa) with the mid-crustal storage region indicated by clinopyroxene barometry (370–490 MPa) indicates that these results are a reasonable estimate.

**5. Discussion**

These results are the first attempt to model pressures and temperatures of magma crystallisation below Ambrym volcano, and add to the sparse but growing body of data on processes operating below persistently active lava lake volcanoes.

Mineral-melt barometry indicates two major crystallisation regions, around 24–29 km and 11–18 km depth. The shallower crystallisation range lies within the likely magma storage region detected at 12–21 km by USGS-NEIC seismic data, while the deeper region corresponds almost exactly to the seismic gap at 25–29 km depth (Fig. 3b).

**Table 4**  
Clinopyroxene thermobarometry results for H<sub>2</sub>O-independent models, with conversion of calculated pressures to depth  $h$  ( $=P/\rho g$ ), assuming a crustal density  $\rho$  of 2700 kg m<sup>-3</sup>.

	Putirka et al., 2003			Eq. 32d		Eq. 32a	
	$K_D$	T (°C)	P (MPa)	T (°C)	P (MPa)		
<b>2005 whole rock/phenocrysts, n = 31</b>							
Mean	0.27 (0.01)	1139 (2)	390 (19)	1171 (5)	414 (59)		
h (km)			15 (1)		16 (2)		
<b>2005 glass/phenocrysts, n = 3</b>							
Mean	0.24 (0.00)	1136 (3)	368 (39)				
h (km)			14 (1)				
<b>2007 whole rock/phenocrysts, n = 3</b>							
Mean	0.26 (0.01)	1140 (2)	410 (22)	1171 (4)	402 (28)		
h (km)			16 (1)		15 (1)		
<b>2007 glass/phenocrysts, n = 1</b>							
Mean	0.25	1147	430				
h (km)			16				

Depth values are rounded to the nearest kilometre. 'Cpx-only' results relate to phenocryst compositions only and include all phenocryst analyses. Values given in this table represent mean  $\pm 1\sigma$  for n clinopyroxene-melt pairs or clinopyroxene-only analyses. Numbers in italics represent one standard deviation of n calculations.

**Table 5**  
Clinopyroxene thermobarometry results for H<sub>2</sub>O-dependent models at 0.6 and 1.3 wt.% melt H<sub>2</sub>O, using Putirka (2008) models Eq. 33 and Eq. 30.

n	$K_D^{Fe-Mg}$	H <sub>2</sub> O wt.%	33		30	
			T (°C)	P (MPa)	h (km)	h (km)
2005 WR/ph	31	0.27 $\pm$ 0.01	0.6	1119 (5)	393 (37)	15 (1)
			1.3	1110 (4)	447 (37)	17 (1)
2005 gl/ph	3	0.24 $\pm$ 0.00	0.6	1108 (7)	398 (63)	15 (2)
			1.3	1099 (7)	452 (63)	17 (2)
2007 WR/ph	3	0.26 $\pm$ 0.01	0.6	1114 (2)	432 (25)	16 (1)
			1.3	1104 (2)	485 (25)	18 (1)

WR/ph = whole rock/phenocryst pairs; gl/ph = glass/phenocryst pairs.

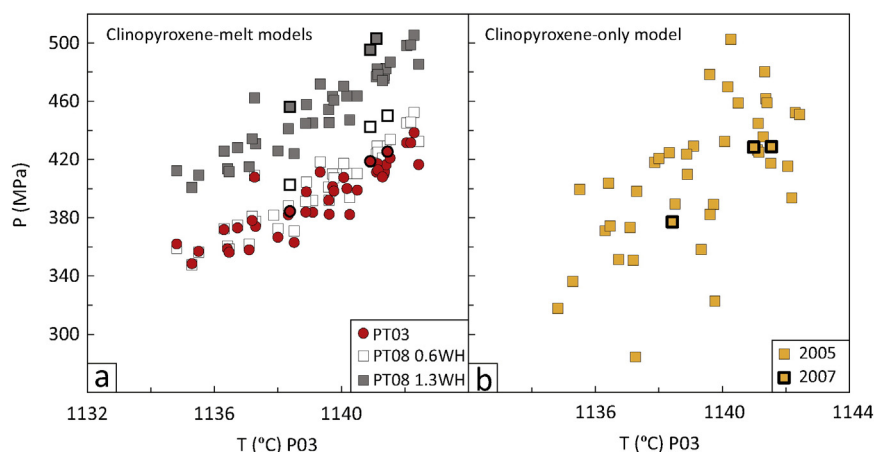


**Fig. 8.** Comparison of results from different barometers used, plotted against temperature values from the Putirka et al. (2003) thermometer. Data marked by symbols of bold outline indicate 2007 reticulite; all other data are from the 2005 scoria. Note that these plots include the entire spread of data, whereas data tables and results cited in the text represent mean values. a) Comparison of clinopyroxene-melt barometry results from the Putirka et al. (2003) barometer (PT03), which is H<sub>2</sub>O-independent, the Putirka (2008) barometer at 0.6 wt.% H<sub>2</sub>O (PT08 0.6WH), and the Putirka (2008) barometer at 1.3 wt.% H<sub>2</sub>O (PT08 1.3WH). Note that PT08 results at 0.6 wt.% H<sub>2</sub>O closely match results from PT03, which has the lowest error and highest precision. This suggests that 0.6 wt.% is a good approximation of water content. b) Results from clinopyroxene-only model 32a (Putirka, 2008).

Thermometry demonstrates that higher-anorthite plagioclase crystallised at temperatures at least 40 °C higher than phenocrystic clinopyroxene, while lower-anorthite plagioclase crystallised close to clinopyroxene crystallisation temperatures, corroborating the indication from barometry that lower-anorthite plagioclase crystallised alongside clinopyroxene. While it may be considered unusual for plagioclase to precede clinopyroxene and olivine, this sequence has been demonstrated experimentally for a basalt of similar composition to that studied here, under similar conditions; i.e. low H<sub>2</sub>O, and low to moderate pressure (Meen, 1990). Previous removal of higher-forsterite olivine is assumed for the samples studied here—post-caldera plagioclase basalts—to bring the magma to this relatively evolved composition, where plagioclase is on the liquidus. In fact, the fractionation models of Picard et al. (1995) postulate generation of the post-caldera plagioclase basalt in a three-stage process, with removal of olivine and augite in the earliest stage, followed by plagioclase-dominated crystallisation at later stages.

Following identification of the locations and conditions of crystallisation, geochemistry and petrography can illustrate the processes operating in these regions. The persistence of the predominant magma and mineral compositions since the early stages of volcanism suggests a stable and homogeneous magma supply (cf. Harris et al., 1999). Rounded, fritted cores or zones in plagioclase record at least one major dissolution event (e.g., thermal or chemical disequilibrium; Clynnne, 1999; Murphy et al., 2000), followed by an uninterrupted period of overgrowth of 200–500 µm of clear plagioclase. Phenocrysts lacking fritted zones perhaps represent the same growth period as the clear rims of the fritted population.

The presence of both euhedral and rounded clinopyroxene and olivine phenocrysts (of similar or identical composition) suggests circulation of more mature phenocrysts into regions where they encounter disequilibrium. Heavily rounded clinopyroxene tends to be associated with large plagioclase glomerocrysts, while the euhedral phenocrysts occur alone, which illustrates that clinopyroxene composition has

remained constant from more texturally mature glomerocrysts to apparently recent euhedral phenocrysts.

This phenocryst convection may be a result of sinking of degassed magma from the surface (e.g. Kazahaya et al., 1994), mixing between resident and recharge magma, or a combination of both (e.g. Jaupart and Vergnolle, 1989; Kazahaya et al., 1994). Latent heat of crystallisation may also play a role (Couch et al., 2001).

Allard et al. (2015) concluded that convective overturn is required to account for observed degassing patterns, based on comparison between pre-eruptive dissolved volatiles and gas plume composition. In their proposed model, gas-rich magma rises to the top of the conduit, degasses at a very shallow level, and sinks back due to increased density following gas loss. Due to low initial H<sub>2</sub>O, the basaltic magma at Ambrym cannot reach the permeability threshold required for degassing until very low pressure (~10 MPa, or ~0.4 km). The prodigious amount of degassing evident in the plume, with extremely minor emission of silicate material, necessarily implies the production of large volumes of degassed magma in the shallow system. Density contrast between dense degassed magma and fresh gas-rich magma drives can be accommodated via convective overturn in order for the system to feed the persistent heavy gas plume. Polacci et al. (2012) found textural evidence of such a process, with two simultaneously-erupted scoria types of low-to-moderate vesicularity and high vesicularity (of identical composition

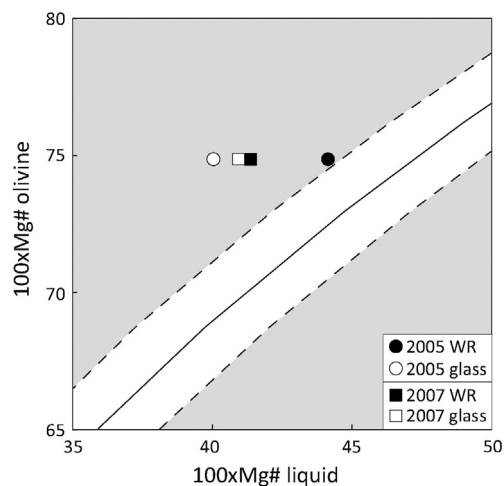


**Fig. 9.** Rhodes diagram showing equilibrium  $K_D^{\text{Fe-Mg}}$  curve of 0.299 (solid line) and error limits of  $\pm 0.053$  (dashed lines) as determined by Putirka (2008).

**Table 6**

KD values for olivine/melt pairs, using the classic ('unadjusted'), alkali-adjusted (Toplis, 2005), and NBO/T-adjusted ('K&W': Kushiuro and Walter, 1998) calculations.

		n	Unadjusted	Toplis	K&W
2005	WR	6	0.44	0.30	0.29
	Glass	3	0.37	0.30	0.30
2007	WR	6	0.40	0.30	0.29
	Glass	3	0.39	0.30	0.30

**Table 7**

Results of olivine-liquid thermometry (Eq. (22), Putirka, 2008), using the average of 28 olivine analyses ( $FO_{74.9 \pm 0.4}$ ) and mean values for glass and whole rock as nominal liquids ( $\mu^{XRF}$  and  $\mu^{EPMA}$ ). Results are rounded to three significant figures.

		Input P (MPa)		T (°C)		
				n	0.6 wt.% H <sub>2</sub> O	1.3 wt.% H <sub>2</sub> O
2005	WR	400	$\mu^{XRF}$	1120	1110	
	Glass	100	$\mu^{EPMA}$	1110	1090	
2007	WR	400	$\mu^{XRF}$	1110	1100	
	Glass	100	$\mu^{EPMA}$	1110	1100	

and comparable crystal content), representing degassed and gas-rich magma respectively.

#### 5.1.1.1. Plumbing model

We propose a model of the magma storage system beneath Ambrym based on a combination of new results and previous data, illustrated in Fig. 11 below. Seismic data and mineral-melt equilibria indicate significant crystallisation at two depths; one near the suggested depth of the Moho for Vanuatu (Coudert et al., 1984; McCall et al., 1970), and one at mid-crustal levels. This concurs with indications of active regions at similar depths from USGS earthquake records. Possible structural controls on the location of the crustal storage region are not known; it may relate to the base of the volcanic pile and attendant lithological and density contrasts. Melt inclusion entrapment pressures (Allard et al., 2015) suggest a potential region of storage and crystallisation at around 3–5 km depth. Low temperatures from olivine-melt thermometry are congruent with this model of shallow crustal crystallisation of olivine.

Petrographic textures seen in phenocrysts from the mid-crustal storage region suggests magma convection at this depth; studies of textural features (Polacci et al., 2012) and degassing processes (Allard et al., 2015) suggest that this is driven by sinking of degassed magma from the shallow conduit.

The model for the magma plumbing system illustrated in Fig. 11 is described as follows:

1. Relatively primitive magma, bearing plagioclase of  $An_{>80}$ , stalls near the crust/mantle interface at ~24–29 km depth, where plagioclase rims of  $An_{63-80}$  overgrow the more primitive cores.
2. Crystallisation, or heat and volatile input following magma recharge, drives further ascent via density reduction.

**Table 8**

Plagioclase thermobarometry results, with conversion of calculated pressures to depth  $h$  ( $=P/\rho g$ ), assuming a crustal density  $\rho$  of 2700 kg m<sup>-3</sup>. Values given represent the mean of  $n$  calculations, with  $1\sigma$  in parentheses.

	0.6 wt.% H <sub>2</sub> O		1.3 wt.% H <sub>2</sub> O	
	T (°C)	P (MPa)	T (°C)	P (MPa)
<i>2005 whole rock, <math>K_D = 0.26 \pm 0.04</math>, <math>n = 65</math></i>				
Mean ( $1\sigma$ )	1170 (2)	720 (40)	1150 (2)	630 (30)
$h$ (km)	–	27 (1)	–	24 (1)
<i>2005 glass, <math>K_D = 0.21 \pm 0.02</math>, <math>n = 63</math></i>				
Mean ( $1\sigma$ )	1140 (2)	420 (30)	1110 (2)	340 (30)
$h$ (km)	–	16 (1)	–	13 (1)
<i>2007 whole rock, <math>K_D = 0.23 \pm 0.07</math>, <math>n = 4</math></i>				
Mean ( $1\sigma$ )	1160 (4)	510 (70)	1140 (4)	420 (60)
$h$ (km)	–	19 (3)	–	16 (2)
<i>2007 glass, <math>K_D = 0.22 \pm 0.03</math>, <math>n = 2</math></i>				
Mean ( $1\sigma$ )	1140 (2)	380 (40)	1110 (2)	300 (30)
$h$ (km)	–	14 (1)	–	11 (1)

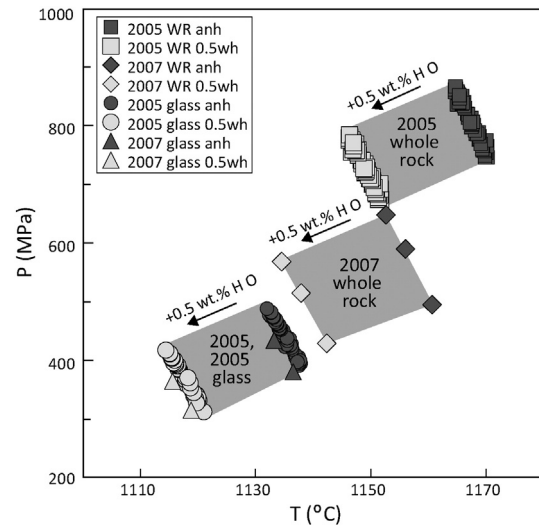


**Fig. 10.** Results of plagioclase-melt thermobarometry. Note that these plots include the entire spread of data, whereas data tables provide mean values. Temperature results are from Eq. 24a of Putirka (2008); pressure results are calculated using the model of Putirka (2005). In 2005 scoria,  $An_{56-72}$  plagioclase records mid-crustal pressures (312–488 MPa; 12–18.4 km), while  $An_{63-80}$  plagioclase crystallised at deeper levels (674–868 MPa; 25.4–32.8 km). The 2007 scoria records shallower depths for higher-anorthite plagioclase ( $An_{64-78}$ ) with whole rock as nominal liquid (429–648 MPa; 16.2–24.5 km) but closely similar depths for lower-anorthite plagioclase ( $An_{64-68}$ ) with glass as liquid (314–434 MPa; 11.9–16.4 km). Standard errors of estimate for these models are  $\pm 36$  °C and  $\pm 247$  MPa ( $\sim 9$  km).

3. The magma stalls again around 11–18 km, where clinopyroxene and lower-anorthite ( $An_{72-56}$ ) plagioclase crystallisation occurs; the upper level of this storage region may correspond to the base of the volcanogenic crust (cf. Collot and Fisher, 1988). The magma composition at this depth is effectively the same as that of the final erupted scoria, as indicated by clinopyroxene-hosted melt inclusion compositions.
4. Since the residual melt evolves no further, buoyancy imparted by thermal and/or volatile recharge, rather than fractionation-induced density reduction, is the presumed impetus for further ascent. The error margins on mineral-melt barometry, and tendency of late-stage minerals to undergo non-equilibrium growth, precludes distinction of crystallisation pressures at such shallow levels. Melt inclusion entrapment pressures indicate that olivine crystallises at low pressures (70 to 100 MPa, or ~3–5 km depth; Allard et al., 2015), which may indicate a further ponding region at such depths. The lower temperatures indicated by olivine thermometry are congruent with this model. Near-surface tremor at ~3.5–3.7 km depth (Legrand et al., 2005) may represent magma or fluid transport related to this crystallisation region.

## 6. Conclusions

Mineral-melt equilibria record crystallisation of clinopyroxene and labradoritic plagioclase ( $An_{72-56}$ ; 51% of plagioclase analyses) phenocrysts at a mid-to-lower-crustal level (11–18 km), within a probable magma storage region previously indicated by seismic data (USGS-NEIC data; Blot, 1981). Bytownitic to labradoritic plagioclase ( $An_{80-63}$ ; 63% of plagioclase analyses) crystallises near the crust/mantle interface (24–29 km), closely corresponding to an intermediate-depth storage region indicated by USGS seismic data and identified by Blot (1981). Plagioclase cores are more primitive than the near-Moho composition, and are presumed to derive from a parental mantle melt. Thermometry results demonstrate that the highest-anorthite plagioclase is the highest-temperature phase, and thus the earliest-crystallising phase

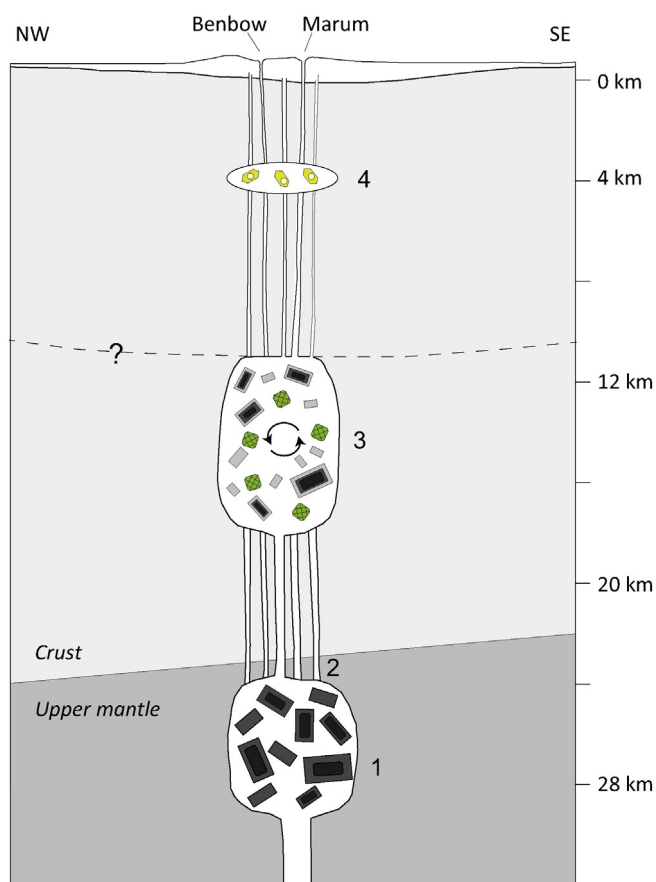


**Fig. 11.** Schematic model of the plumbing system of Ambrym based on mineral-melt thermobarometry. The location of the base of the crust is based on gravity data which indicates an inclined boundary from 20.8 km on the eastern side of the island to 24.8 km on the western side (McCall et al., 1970). The dashed line represents a hypothetical structural discontinuity at the upper limit of the mid-crustal storage region indicated by clinopyroxene and medium-anorthite plagioclase barometry. The ‘magma chamber’ type storage regions depicted are a simplification for the purposes of illustration and are not intended to suggest that large-scale chambers are present in such a form. In plagioclase phenocrysts depicted, the darkest cores represent the most anorthitic, which  $K_D$  calculations indicate derived from a more mafic melt than the typical central vent basalt. Medium grey denotes  $An_{63-80}$  plagioclase crystallised in the sub-Moho storage region. The palest grey plagioclase is that crystallised in the mid-crust, as microphenocrysts and overgrowth on more primitive plagioclase. Depth is calculated assuming an average density of  $2700 \text{ kg m}^{-3}$ . Numbers 1–4 correspond to numbered stages described in the text.

represented in the central vent basaltic magma, followed by the near-Moho plagioclase, and then approximately coeval clinopyroxene and lower-anorthite plagioclase at lower- to mid-crustal depths, with  $Fe_{75}$  olivine crystallising at a late stage.

Occurrence of the deep plagioclase crystallisation region near the estimated level of the crust/mantle interface suggests a structural control on magma ascent at this level. Potential structural influences on shallower crystallisation regions are uncertain due to scarcity of data on the structure of the lithosphere below Ambrym.

Petrographic observations provide support for the convective model of magma supply at persistently active lava lake volcanoes, whereby magma rises, degasses, and recirculates downward into the storage region at depth. Textural indications of circulation in phenocrysts associated with the mid-to-shallow-crustal storage region and presence of deeper-derived mineralogy (bytownitic plagioclase) only as a relict/antecrystic phase indicates that the mid- to shallow crust is where magma convection occurs.

This study demonstrates that the combination of petrographic and thermobarometric study can illustrate both the processes and conditions of magma storage beneath a volcanic system.

## Acknowledgements

I thank Dr. Keith Putirka for input on the use of thermobarometry models. This work has been supported by the Natural Environment Research Council (NERC) (NE/E529376/1) through a NERC studentship to FS.

## References

- Allard, P., Behncke, B., D’Amico, S., Neria, M., Gambino, S., 2006. Mount Etna 1993–2005: anatomy of an evolving eruptive cycle. *Earth Sci. Rev.* 78, 85–114.
- Allard, P., Aiuppa, A., Bani, P., Métrich, N., Bertagnini, A., Gauthier, P.J., Shinohara, H., Sawyer, G., Parello, F., Bagnato, E., Pelletier, B., Garaebiti, E., 2015. Prodigious emission rates and magma degassing budget of major, trace and radioactive volatile species from Ambrym basaltic volcano, Vanuatu island Arc. *J. Volcanol. Geotherm. Res.* (Available online 3 September 2015).
- Bani, P., Oppenheimer, C., Tsanev, V.I., Crimp, R., Cronin, S., Calkins, J., Charley, D., Lardy, M., 2009. Surge in sulphur and halogen degassing from Ambrym volcano, Vanuatu. *Bull. Volcanol.* 10, 1159–1168.
- Bani, P., Vergnolle, S., Zielinski, C., Lardy, M., Le Pichon, A., Ponceau, D., Gallois, F., Herry, P., Todman, S., Garaebiti, E., 2010. Probing the magma plumbing of Ambrym volcano, by a triangular acoustic network. *Geophys. Res. Abstr.* 12 (EGU2010-6781, EGU General Assembly 2010).
- Bani, P., Oppenheimer, C., Allard, P., Shinohara, H., Tsanev, V., Carn, S., Garaebiti, E., 2012. First estimate of volcanic  $SO_2$  budget for Vanuatu island arc. *J. Volcanol. Geotherm. Res.* 211, 36–46.
- Bertagnini, A., Di Roberto, A., Pompilio, M., 2011. Paroxysmal activity at Stromboli: lessons from the past. *Bull. Volcanol.* 73, 1229–1243.
- Blot, C., 1981. Deep root of andesitic volcanoes: new evidence of magma generation at depth in the Benioff zone. *J. Volcanol. Geotherm. Res.* 10, 339–364.
- Clynne, M., 1999. A complex magma mixing origin for rocks erupted in 1915, Lassen Peak, California. *J. Petrol.* 40, 105–132.
- Collot, J.-Y., Fisher, M.A., 1988. Crustal structure, from gravity data, of a collision zone in the central New Hebrides island arc. In: Greene, H.G., Wong, F.L. (Eds.), *Geology and Offshore Resources of Pacific Islands Arcs—Vanuatu Region* Earth Science Ser. Vol. 8. Circum-Pacific Council for Energy and Mineral Resources, Houston, TX, pp. 125–139.
- Couch, S., Harford, C.L., Sparks, R.S.J., Carroll, M.R., 2001. Mineral disequilibrium in lavas explained by convective self-mixing in open magma chambers. *Nature* 411, 1037–1039.
- Coudert, E., Cardwell, R.K., Isacks, B.L., Chatelain, J.-L., 1984. *Bull. Seismol. Soc. Am.* 74, 913–924.
- Cronin, S.J.S., Sharp, D.S., 2002. Environmental impacts on health from continuous volcanic activity at Yasur (Tanna) and Ambrym, Vanuatu. *Int. J. Environ. Health Res.* 12, 109–123.
- Danyushevsky, L.V., Plechov, P., 2011. Petrolog3: integrated software for modeling crystallization processes. *Geochem. Geophys. Geosyst.* 12 (7).
- Eissen, J.P., Blot, C., Louat, R., 1991. Chronology of the historic volcanic activity of the New Hebrides island arc from 1595 to 1991: ORSTOM Rapports Scientifiques et Technique, Sciences de la Terre. *Géologie-Géophysique* 2 (69 p).
- Falloon, T.J., Green, D.H., 1988. Anhydrous partial melting of peridotite from 8 to 35 Kb and the petrogenesis of MORB. *J. Petrol. Spec. Lithosphere Issue* 379–414.
- Falloon, T.J., Hutton, C.J., Harris, L., 1988. Anhydrous partial melting of a fertile and depleted peridotite from 2 to 30 Kb and application to basalt petrogenesis. *J. Petrol.* 29, 1257–1282.
- Francis, P.W., Oppenheimer, C., Stevenson, D.S., 1993. Endogenous growth of persistently active volcanoes. *Nature* 366, 544–557.
- Gorton, M.P., 1977. The geochemistry and origin of Quaternary volcanism in the New Hebrides. *Geochim. Cosmochim. Acta* 41, 1257–1270.
- Greene, H.G., Macfarlane, A., Johnson, D.P., Crawford, A.J., 1988. Structure and tectonics of the central New Hebrides arc. In: Greene, H.G., Wong, F.L. (Eds.), *Geology and Offshore Resources of Pacific Islands Arcs—Vanuatu Region*. Circum-Pacific Council for Energy and Mineral Resources Earth Science Series Vol. 8, pp. 377–412.
- Gregory, J.W., 1917. The Ambrym eruptions of 1913–14. *Geol. Mag.* 4, 529–540.
- Global Volcanism Program, 2013. In: Venzke, E. (Ed.), *Volcanoes of the World* v. 4.4.1. Smithsonian Institution. <http://dx.doi.org/10.5479/si.GVP.VOTW4-2013> (Downloaded 14 Nov 2015).
- Harris, A.J.L., Flynn, L.P., Rothery, D.A., Oppenheimer, C., Sherman, S.B., 1999. Mass flux measurements at active lava lakes: implications for magma recycling. *J. Geophys. Res.* 104, 7117–7136.
- Harris, A., Ripepe, M., 2007. Temperature and dynamics of degassing at Stromboli. *J. Geophys. Res.* 112, B03205. <http://dx.doi.org/10.1029/2006JB004393>.
- Harris, A.J.L., Stevenson, D.S., 1997. Magma budgets and steady-state activity of Vulcano and Stromboli. *Geophys. Res. Lett.* 24, 1043–1046.
- Huebner, J.S., Sato, M., 1970. The oxygen fugacity–temperature relationships of manganese oxide and nickel oxide buffers. *Am. Mineral.* 55, 934–952.
- Jaques, A.L., Green, D.H., 1980. Anhydrous melting of peridotite at 0–15 Kbar pressure and the genesis of tholeiitic basalts. *Contrib. Mineral. Petrol.* 73, 287–310.
- Jaupart, C., Vergnolle, S., 1989. The generation and collapse of a foam layer at the roof of a basaltic magma chamber. *J. Fluid Mech.* 203, 347–380.
- Kazahaya, K., Shinohara, H., Saito, G., 1994. Excessive degassing of Izu–Oshima Volcano: magma convection in a conduit. *Bull. Volcanol.* 56, 207–216.

- Kress, V.C., Carmichael, I.S.E., 1991. The compressibility of silicate liquids containing  $\text{Fe}_2\text{O}_3$  and the effect of composition, temperature, oxygen fugacity and pressure on their redox states. *Contrib. Mineral. Petrol.* 108, 82–92.
- Kushiro, L., Walter, M.J., 1998. Mg–Fe partitioning between olivine and mafic-ultramafic melts. *Geophys. Res. Lett.* 25, 2337–2340.
- Le Bas, M.J., le Maitre, R.W., Streckeisen, A., Zanettin, B., 1986. A chemical classification of volcanic rocks based on the total alkali–silica diagram. *J. Petrol.* 27, 745–750.
- Legrand, D., Rouland, D., Frogneux, M., Carniel, R., Charley, D., Roullet, G., Robin, C., 2005. Interpretation of very long period tremors at Ambrym volcano, Vanuatu, as quasi-static displacement field related to two distinct magmatic sources. *Geophys. Res. Lett.* 32, L06314.
- Marsh, B.D., 2013. On some fundamentals of igneous petrology. *Contrib. Mineral. Petrol.* 166, 665–690.
- McCull, G.J.H., LeMaitre, R.W., Malahoff, A., Robinson, G.P., Stephenson, P.J., 1970. The geology and geophysics of the Ambrym Caldera, New Hebrides. *Bull. Volcanol.* 34, 681–696.
- Meen, J.K., 1990. Elevation of potassium content of basaltic magma by fractional crystallization: the effect of pressure. *Contrib. Mineral. Petrol.* 104, 309–331.
- Murphy, M.D., Sparks, R.S.J., Barclay, J., Carroll, M.R., Brewer, T.S., 2000. Remobilisation of andesite magma by intrusion of mafic magma at the Soufrière Hills volcano, Montserrat, West Indies. *J. Petrol.* 11, 21–42.
- Németh, K., Cronin, S.J., 2011. Drivers of explosivity and elevated hazard in basaltic fissure eruptions: the 1913 eruption of Ambrym volcano, Vanuatu (SW-Pacific). *J. Volcanol. Geotherm. Res.* 201, 194–209.
- Oppenheimer, C., Francis, P., 1998. Implications of long-lived lava lakes for geomorphological and plutonic processes at Erta'Ale volcano, Afar. *J. Volcanol. Geotherm. Res.* 80, 101–111.
- Polacci, M., Baker, D.R., La Rue, A., Mancini, L., Allard, P., 2012. Degassing behaviour of vesiculated basaltic magmas: an example from Ambrym volcano, Vanuatu arc. *J. Volcanol. Geotherm. Res.* 233, 55–64.
- Picard, C., Monzier, M., Eissen, J.-P., Robin, C., 1995. Concomitant evolution of tectonic environment and magma geochemistry, Ambrym volcano (Vanuatu, New Hebrides arc). In: Smellie, J.L. (Ed.), *Volcanism Associated with Extension at Consuming Plate Margins*. Geological Society of London Special Publication Vol. 81, pp. 135–154.
- Putirka, K.D., 2005. Igneous thermometers and barometers based on plagioclase + liquid equilibria: tests of some existing models and new calibrations. *Am. Mineral.* 90, 336–346.
- Putirka, K.D., 2008. Thermometers and barometers for volcanic systems. In: Putirka, K.D., Topley, F. (Eds.), *Minerals, Inclusions and Volcanic Processes*. Reviews in Mineralogy and Geochemistry Vol. 69, pp. 61–120.
- Putirka, K., Ryerson, F.J., Mikaelian, H., 2003. New igneous thermobarometers for mafic and evolved lava compositions, based on clinopyroxene + liquid equilibria. *Am. Mineral.* 88, 1542–1554.
- Robin, C., Eissen, J.-P., Monzier, M., 1993. Giant tuff cone and 12-km-wide associated caldera at Ambrym volcano (Vanuatu, New Hebrides arc). *J. Volcanol. Geotherm. Res.* 55, 225–238.
- Roeder, P.L., Emslie, R.F., 1970. Olivine–liquid equilibrium. *Contrib. Mineral. Petrol.* 29, 275–289.
- Sack, R.O., Ghiorso, M.S., 1989. Importance of considerations of mixing properties in establishing an internally consistent database: thermochemistry of minerals in the system  $\text{Mg}_2\text{SiO}_4\text{–Fe}_2\text{SiO}_4\text{–SiO}_2$ . *Contrib. Mineral. Petrol.* 102, 41–68.
- Sack, R.O., Ghiorso, M.S., 1991a. An internally consistent model for the thermodynamic properties of Fe–Mg–titanomagnetite–aluminates spinels. *Contrib. Mineral. Petrol.* 106, 474–505.
- Sack, R.O., Ghiorso, M.S., 1991b. Chromian spinels as petrogenetic indicators: thermodynamics and petrological applications. *Am. Mineral.* 76, 827–847.
- Sack, R.O., Ghiorso, M.S., 1994a. Thermodynamics of multicomponent pyroxenes: I. Formulation of a general model. *Contrib. Mineral. Petrol.* 116, 277–286.
- Sack, R.O., Ghiorso, M.S., 1994b. Thermodynamics of multicomponent pyroxenes: II. Phase relations in the quadrilateral. *Contrib. Mineral. Petrol.* 116, 287–300.
- Sack, R.O., Ghiorso, M.S., 1994c. Thermodynamics of multicomponent pyroxenes: III. Calibration of  $\text{Fe}^{2+}(\text{Mg})^{-1}$ ,  $\text{TiAl}(\text{MgSi})^{-1}$ ,  $\text{TiFe}^{3+}(\text{MgSi})^{-1}$ ,  $\text{AlFe}^{3+}(\text{MgSi})^{-1}$ ,  $\text{NaAl}(\text{CaMg})^{-1}$ ,  $\text{Al}_2(\text{MgSi})^{-1}$  and  $\text{Ca}(\text{Mg})^{-1}$  exchange reactions between pyroxenes and silicate melts. *Contrib. Mineral. Petrol.* 118, 271–296.
- Scordilis, E.M., 2006. Empirical global relations converting  $M_s$  and  $m_b$  to moment magnitude. *J. Seismol.* 10, 225–236.
- Sides, I., Edmonds, M., MacLennan, J., Houghton, B.F., Swanson, D.A., Steele-MacInnis, M.J., 2014. Magma mixing and high fountaining during the 1959 Kīlauea Iki eruption, Hawai'i. *Earth Planet. Sci. Lett.* 400, 102–112.
- Topley, M.J., 2005. The thermodynamics of iron and magnesium partitioning between olivine and liquid: criteria for assessing and predicting equilibrium in natural and experimental systems. *Contrib. Mineral. Petrol.* 149, 22–39.
- Vanuatu National Statistics Office, 2009. National Census of Population and Housing. (Retrieved June 27, 2015, from <http://www.vnsso.gov.vu/index.php/component/advlisting/?view=download&filed=1996>).
- Vergnolle, S., Zielinski, C., Bani, P., Lardy, M., Le Pichon, A., Ponceau, D., Millier, P., Gallois, F., Herry, P., Todman, S., Garaebiti, E., 2013. Listening to Ambrym volcano (Vanuatu), by a triangular acoustic network: a precursor to a Strombolian episode [abstract]. Proceedings of the International Association of Volcanology and Chemistry of the Earth's Interior (IAVCEI) General Assembly, Kagoshima, Japan, abstract 3A1\_2A-07, p. 246.
- Witham, C.S., 2005. Volcanic disasters and incidents: a new database. *J. Volcanol. Geotherm. Res.* 148, 191–233.
- Wood, B.J., 1991. Oxygen barometry of spinel peridotites. In: H., Lindsley D. (Ed.), *Oxide Minerals: Petrologic and Magnetic Significance*. Mineralogical Society of America, Washington D.C., pp. 417–431.
- Wright, R., Pilger, E., 2008. Radiant flux from Earth's subaerially erupting volcanoes. *Int. J. Remote Sens.* 29, 6443–6466.